Numerical simulations of flame spread in pine needle beds using simple thermal decomposition models

Numerical simulations of flame spread in pine needle beds using simple thermal decomposition models

Eric V. Mueller[a*], Zakary Campbell-Lochrie[b], Carlos Walker-Ravena[b], Rory M. Hadden[b]

[a] Fire Research Division, National Institute of Standards and Technology, Gaithersburg, MD, USA, eric.mueller@nist.gov

[b] School of Engineering, University of Edinburgh, Edinburgh, UK

[*] Corresponding author

Highlights:

- A multiphase CFD model was used to simulate flame spread in pine needles in still air
- Fitting the pyrolysis model with fuel species specific data impacted burning rate
- An updated char oxidation model was shown to provide reasonable results
- The model was able to capture fuel structure effects on spread and heat transfer

Abstract:

Computational fluid dynamics (CFD) models have increased in use for studying scenarios relevant to wildland fires, such as examination of the driving processes in flame spread in vegetative fuels. However, these tools utilize a complex set of submodels which require a large number of input parameters. Often the full set of fuel-specific parameters are not well-quantified and the user must rely upon the best available information. In this study, we examine the implications of using different simple models for thermal decomposition when simulating flame spread through a bed of dead pine needles in quiescent conditions. Model results using one set of common literature values are compared to those using data from milligram-scale characterizations of the fuel. An updated model for char oxidation is also implemented and tested. It was found that the literature values over-predicted mass loss rate by a factor of 2.4, while the fuel-specific values yielded predictions within the experimental uncertainty. A simple approach to decomposition modeling was also shown to be useful for investigating the role of bed structure on flame spread and the heat flux within the fuel bed.

Keywords: wildfires; flame spread; modeling; CFD

1. Introduction

Quantifying and mitigating the impact of wildland fires is a complex, multi-scale problem. Large uncontrolled wildland and wildland-urban interface (WUI) fires have been increasing in severity in recent years. However, understanding the behavior and impact of prescribed fires, which may occur at different spatial and temporal scales, is equally important for informing long-term solutions. Therefore, it is necessary to have robust engineering tools which allow the exploration of different scenarios, ranging from the evaluation of the impact of wildland and WUI fires to the planning of prescribed fires.

In recent years, detailed computational fluid dynamics (CFD) models, typically employing a

multiphase formulation [1–3], have emerged as one such tool for investigating the driving processes of various phenomena related to wildland fires. The use of this technique has been described in several reviews of wildland fire modeling [4–6]. In a number of cases, efforts have been made to evaluate these models against detailed experimental measurements (i.e. beyond spread rate) as the quality of the models depend on their ability to predict underlying physical phenomena which dictate global fire behavior. Such models have been compared to experimental data related to the burning of individual plants [7, 8], ignition and flame spread in simple fuels beds (pine needles, excelsior, wood sticks) at laboratory scale [9–14], and more complex fuel beds at field scale [15]. Nevertheless, this approach for modeling flame spread in natural fuels requires a wide range of detailed input parameters, and the models are still in need of a considerable degree of testing and validation.

One of the challenges for this type of CFD modeling is providing an adequate description of the mechanisms involved in the thermal decomposition of vegetative material. Typically, this decomposition is assumed to involve three main steps: drying, pyrolysis, and char oxidation. [1, 16]. A number of studies have focused on the fundamental description of these processes in vegetation — particularly pyrolysis [e.g. 17, 18]. In a few cases, these detailed models have been applied to the full CFD approach. Borujerdi et al. [19] used a ten-reaction pyrolysis model in the simulation of the burning of a single leaf. Leventon and Bruns [20] fit a pyrolysis model with three reactions to data from a variety of foliage and stem samples and tested the sensitivity when applying these models to simulations of grass fires. Often the main reactions are assumed to be related to cellulose, hemicellulose, and lignin but the details are more complex [21]. Ahmed et al. [14] also used a three-component pyroylsis model to simulate flame spread through pine wood sticks. In many cases, however, very detailed species-specific characterization of the decomposition mechanisms are not available and it also may not be practical to calibrate complex decomposition models to every possible fuel type. The alternative is to rely upon literature values. Indeed, many studies have employed simple one-step models, often with the same set of constants. For this reason, it is worth exploring the sensitivity to this generalized approach.

In this study we quantify the potential sensitivity of a CFD model to the application of simple thermal decomposition models when simulating flame spread through a bed of pine needles under quiescent (no-wind) conditions [22]. We are able to leverage the fact that recent work has helped to parameterize submodels for drag and convection in these fuel beds [23, 24]. A set of commonly applied models to describe drying, pyrolysis, and char oxidation was used and compared to experimental flame spread data. The model coefficients were then tuned to milligram-scale measurements which are specific to the species under investigation. In addition, an updated model for char oxidation, based on a mass transport principle, was implemented. In this way, the study builds upon previous simulations in similar fuel beds which do not consider these adaptations of the thermal decomposition. After quantifying the role of these simple models, the model was also evaluated for its ability to predict flame spread as a function of fuel bed properties and for the prediction of heat fluxes.

2. Materials and Methods

2.1 Experimental measurements

The numerical simulations described in this work were based on the experimental data of Campbell-Lochrie et al. [22, 25]. In this work, the effects of fuel bed structure on flame spread in pine needles under quiescent conditions were examined in detail. Due to the absence of applied wind, the flow through the fuel bed and the impact of structure was driven by buoyancy of the plume. Experiments were conducted on a fuel bed measuring 1.50 m x 0.67 m (with a variable depth), and comprised of dead *Pinus rigida* (pitch pine) needles. The bed was supported by a vermiculite table and sidewalls were set such that they extended 3 cm above the fuel height to restrict lateral entrainment. Flame spread was initiated by igniting an acetone soaked wick at one end of the bed. An example of one such experiment is shown in Fig. 2. In this study we focused on several experimental measurements which are valuable for model comparison. These were:

- Mass loss rate, measured by a load cell under the table;
- Flame spread rate, measured by video analysis; and
- Radiative heat flux, measured by sapphire-windowed, water-cooled heat flux gauges (i.e. radiometers) pointed upward from the table surface. Measurements were adjusted to account for the 85 % transmissivity of the sapphire window.

2.2 Numerical model

Simulations of flame spread in the pine needle beds were carried out using the National Institute of Standards and Technology (NIST) Fire Dynamics Simulator (FDS) version 6.7.9 [26]. This CFD model employs a large eddy simulation approach for solving a low-Mach number formulation of the Navier-Stokes equations. The conservation equations are approximated by finite differences, applied on a three-dimensional, rectilinear grid. Thermal radiation is computed using a finite volume technique. In this case, combustion is modeled as mixing-controlled with infinitely fast chemistry, using the eddy dissipation concept. We assume a single gas-phase reaction with a prescribed heat of combustion, soot yield, and radiative fraction, as described in Section 2.3. A full presentation of the model details, particularly of the gas-phase solution, is beyond the scope of this paper but can be found in the documentation [26, 27]. A good summary has also been given in a recent paper by Vanella et al. [28].

In FDS, subgrid-scale vegetation can be incorporated with source and sink terms in the gas-phase conservation equations and the radiation transport equation through a multiphase formulation — in particular by using Lagrangian particles as surrogates to represent the vegetation within a given volume. Using this approach, the solid phase is assumed to be highly disperse such that porosity effects are neglected in the gas-phase and flow is modeled with the superficial velocity [23]. Relevant details of the multiphase formulation as used to describe the vegetative fuel bed in this study are presented below.

2.2.1 Momentum and heat transfer

The effect of bed drag on the surrounding fluid flow is represented with a bulk volumetric drag force in the gas-phase momentum equation [23]:

$$\mathbf{f_b} = \frac{\rho}{2} c_\mathrm{d} c_\mathrm{s} \sigma_\mathrm{s} \beta \mathbf{u} \|\mathbf{u}\|, \tag{1}$$

where c_d is a fuel particle drag coefficient, c_s is a shape factor, σ_s is the particle surface-to-volume ratio, and β is the fuel bed packing ratio. Following a previous investigation of flow through the same type of fuel bed, a Reynolds-dependent drag coefficient was used [29]:

$$c_\mathrm{d} = \begin{cases} \dfrac{10}{\mathrm{Re}_\mathrm{p}^{0.8}}, & \mathrm{Re}_\mathrm{p} \leq 1 \\ \dfrac{10}{\mathrm{Re}_\mathrm{p}}(0.6 + 0.4\,\mathrm{Re}_\mathrm{p}^{0.8}), & 1 < \mathrm{Re}_\mathrm{p} < 1000 \\ 1.0, & \mathrm{Re}_\mathrm{p} \geq 1000, \end{cases} \tag{2}$$

where Re_p is a particle Reynolds number, $\mathrm{Re}_\mathrm{p} = 4u/\sigma_\mathrm{s}\nu$. For the shape factor, a value of $c_\mathrm{s} = 0.16$ was used to approximate projected area from surface area [23].

In this particular scenario, fuel particles (pine needles) were assumed to behave as thermally thin. The energy equation for a particle can then be written as:

$$\rho_\mathrm{s}\, c_\mathrm{p,s}\, \frac{\mathrm{d}T_\mathrm{s}}{\mathrm{d}t} = h_\mathrm{c}\sigma \left(T_\mathrm{g} - T_\mathrm{s}\right) + \epsilon_\mathrm{s}\sigma_\mathrm{s} \left(\frac{U}{4} - \sigma T_\mathrm{s}^4\right) + \dot{q}_\mathrm{s}''', \tag{3}$$

where the terms on the right-hand side account for convection, radiation, and internal reactions. The solid density, ρ_s, is the sum of the constituent material components, which in this case were taken to be water, dry vegetation, char, and ash. The specific heat, $c_\mathrm{p,s}$, and particle emissivity, ϵ_s, are the weighted sum of the value for each material component. U is the integrated radiation intensity from the gas-phase and σ is the Stefan–Boltzmann constant.

The effect of forced convective heat exchange was represented using a Nusselt number correlation:

$$\mathrm{Nu_F} = 0.417\,\mathrm{Re}_\mathrm{p}^{0.553}\,\mathrm{Pr}^{1/3}, \tag{4}$$

assuming a Prandtl number of $\mathrm{Pr} = 0.7$. This model was taken from a previous investigation of convective heat transfer through the same type of fuel bed [24]. An additional Nusselt correlation was used to account for natural convection:

$$\mathrm{Nu_N} = \left(0.6 + 0.321\,\mathrm{Ra}^{1/6}\right)^2. \tag{5}$$

For any given time step, the convective heat transfer coefficient is taken as the maximum value from these two correlations:

$$h_\mathrm{c} = \frac{k\sigma_\mathrm{s}}{4} \max\left\{\mathrm{Nu_N}, \mathrm{Nu_F}\right\}, \tag{6}$$

where k is the thermal conductivity of the gas.

2.2.2 Mass transfer

Tracking the evolution of solid-phase mass is required both for computing exchanges with the gas phase and for evaluating the effect of any reactions on the solid-phase energy equation. Following previous studies, the thermal decomposition of the solid fuel is broken up into three single-reaction steps: drying (endothermic), pyrolysis (endothermic), and char oxidation (exothermic). More complex mechanisms have been considered for natural fuels (typically wood). These include multi-step reactions as well as the potential for exothermic oxidative pyrolysis. However, the focus here is on the description of these three main mechanisms. The evolution of the solid mass is determined according to:

$$\frac{\mathrm{d}\rho_\mathrm{s}}{\mathrm{d}t} = -r_{\mathrm{H_2O}} - (1-\nu_\mathrm{char})\, r_\mathrm{pyr} - (1-\nu_\mathrm{ash})\, r_\mathrm{char}, \tag{7}$$

where r_x are the reaction rates. In this case, the drying and pyrolysis may proceed in parallel while the char oxidation occurs in series (char is formed as a product of pyrolysis). The energy source term in Eq. (3) is then:

$$\dot{q}'''_\mathrm{s} = -\Delta h_{\mathrm{H_2O}}\, r_{\mathrm{H_2O}} - \Delta h_\mathrm{pyr}\, r_\mathrm{pyr} - r_\mathrm{char}\left[\Delta h_\mathrm{char} \; - \nu_{\mathrm{O_2,char}}\left(h_{\mathrm{O_2}}(T_\mathrm{g}) - h_{\mathrm{O_2}}(T_\mathrm{s})\right)\right], \tag{8}$$

which depends on the respective heats of reaction, Δh, and any change in sensible enthalpy related to bringing oxygen to the temperature of the solid during char oxidation, $h_{\mathrm{O_2}}$.

A common approach to modeling the reaction rates is to employ Arrhenius kinetics [30]. In this case, the drying rate is:

$$r_{\mathrm{H_2O}} = \rho_{\mathrm{s,H_2O}} A_{\mathrm{H_2O}} T_\mathrm{s}^{n_T} \exp\left(-\frac{E_{\mathrm{H_2O}}}{RT_\mathrm{s}}\right) \tag{9}$$

and the pyrolysis rate is:

$$r_\mathrm{pyr} = \rho_{\mathrm{s,dry}} A_\mathrm{pyr} \exp\left(-\frac{E_\mathrm{pyr}}{RT_\mathrm{s}}\right) \tag{10}$$

This requires the determination of kinetic constants, and because the necessary information is often unavailable for specific fuels a considerable number of studies have relied upon previously proposed values for pine needles, established by Porterie et al. [30]. These values are shown in the first column of Table 1 (model DM1).

For this study, thermogravimetric analysis (TGA) data were available for the specific vegetation considered [31]. We use data from 15 mg samples which were heated in air at a rate of 5 K/min and 35 K/min, as shown in Fig. 1. Values of A and E were estimated for drying and pyrolysis by fitting the maximum normalized mass loss rate ($\dot{\mathrm{m}}/\mathrm{m}_0$) and the temperature at which this occurred [26]. Equation (9) was simplified by assuming $n_T = 0$. Note that because the tests were conducted in air, Fig. 1 also shows a third reaction: char oxidation. However, due to uncertainty in the details of the available surface area for this reaction in the TGA this part of the curve was not used for fitting.

It is acknowledged that using this simple approach does not capture the behavior at all heating rates equally well [17, 18]. Therefore, we consider separate fits to each of the heating rates: model *DM2* and *DM3* for 5 K/min and model *DM4* for 35 K/min (Table 1). This is discussed further in Supplementary Material. Future work may extend this analysis to investigate more complex fitting

techniques, such as those which produce conversion-degree dependent coefficients or involve multiple reactions. However, data for different vegetation types are often limited and so the aim here is to explore the sensitivity of the flame spread predictions to fitting the simple model to individual heating rates.

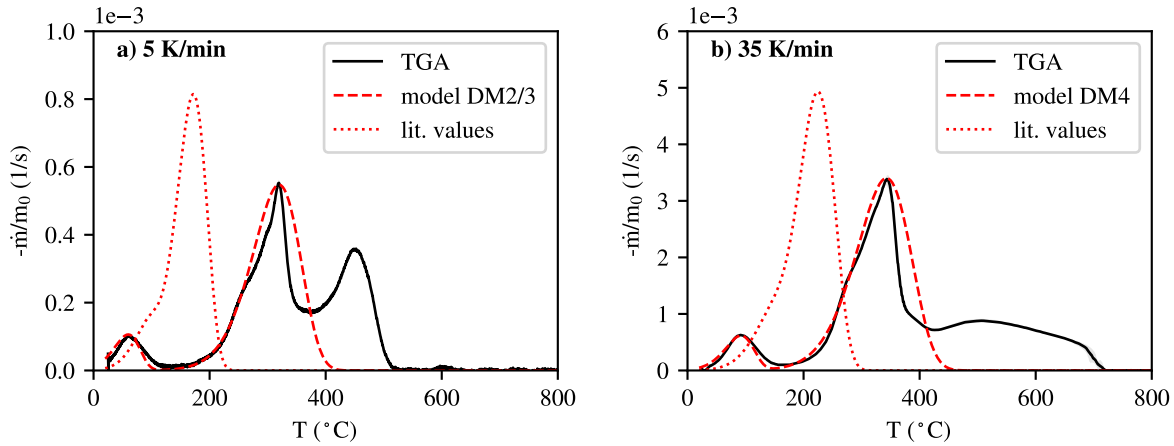

Fig. 1. TGA data compared to modeled response with fit and literature values [30] of kinetic constants for heating rates of a) 5 K/min and b) 35 K/min. Experimental curves are averages of three tests.

In order to model the third reaction of char oxidation, a number of studies have employed the Arrhenius model proposed by Porterie et al. [30]:

$$r_{\text{char}} = \frac{\rho Y_{O_2}}{\nu_{O_2,\text{char}}} \sigma_s A_{\text{char}} \exp\left(-\frac{E_{\text{char}}}{RT_s}\right)\left(1 + \beta_{\text{char}}\sqrt{\text{Re}_p}\right). \tag{11}$$

This model depends on the local density of oxygen (ρY_{O_2}), the mass stoichiometric coefficient of oxygen consumed ($\nu_{O_2,\text{char}}$), the available surface area (σ), and a coefficient to account for the effect that blowing has on enhancing the reaction rate (β_{char}). This approach was used in models *DM1* and *DM2*, with coefficients summarized in Table 1.

This model does not directly consider the sub-grid effects of mass transport, as Y_{O2} is the value in the surrounding gas-phase grid cell (at least in the FDS implementation, and the approach in the original reference is ambiguous). The effect is considered to some degree through the Reynolds-dependent term which enhances the oxidation rate due to a blowing effect. However, the origin of this adjustment and the importance of the value of β_{char} are also not clear.

An alternative approach is to account for the unresolved transport of oxygen to the particle surface more directly. In this case, we borrow from the approach of Boonmee and Quintiere [32] and model the surface oxidation of char as:

$$r_{\text{char}} = Y_{O_2,\text{surf}}\, \sigma_s\, A_{\text{char}} \exp\left(-\frac{E_{\text{char}}}{RT_s}\right), \tag{12}$$

where $Y_{O_2,\text{surf}}$ is the mass fraction of oxygen at the particle surface and A_{char} has units of kg/(m^2 s) (compared to m/s in Eq. (11)). The oxygen mass fraction at the surface is determined by an

estimation of the mass transfer and conservation of mass, assuming any oxygen consumed by the reaction must be supplied through this transport:

$$h_m \ln(B+1) = Y_{O_2,\text{surf}} A_{\text{char}} \exp\left(-\frac{E_{\text{char}}}{RT_s}\right), \tag{13}$$

$$B = \frac{Y_{O_2,\infty} - Y_{O_2,\text{surf}}}{\nu_{O_2,\text{char}} + Y_{O_2,\text{surf}}}, \tag{14}$$

where $h_m = h_c/c_p$ is the mass transfer coefficient and $Y_{O_2,\infty}$ is the oxygen mass fraction in the surrounding grid cell. To solve for $Y_{O_2,\text{surf}}$, we apply the following linear approximation for small values of B [33]:

$$\ln(B+1) \approx B. \tag{15}$$

In this way, a quadratic equation can be solved to obtain $Y_{O_2,\text{surf}}$ and solve Eq. (12). This alternative approach was used for models *DM3* and *DM4*.

The final aspect of decomposition which was modified was the assumed reaction for char oxidation. For models *DM1-4* the mass stoichiometric coefficient of oxygen consumed ($\nu_{O_2,\text{char}}$) and the heat of reaction for char oxidation (Δh_{char}) were taken from [30]. These are lower than the theoretical values for complete combustion of carbon in oxygen [33]. Other models have accounted for incomplete combustion of char as a function of increasing temperature, which also leads to a reduced heat of reaction [10, 11] and such complexity may be considered in future iterations. However, in this case model *DM5* modifies these values to consider an idealized reaction of pure carbon to carbon dioxide (again, summarized in Table 1).

Table 1. Summary of thermal decomposition models tested. References are given where appropriate.

Parameter	***DM1***	***DM2***	***DM3***	***DM4***	***DM5***
A_{H_2O}	600,000 $K^{0.5}$/s [30]	4830 1/s	4830 1/s	25,600 1/s	4830 1/s
E_{H_2O}	48,200 J/mol [30]	39,100 J/mol	39,100 J/mol	42,400 J/mol	39,100 J/mol
n_T	-0.5	0	0	0	0
A_{pyr}	36,300 1/s [30]	1180 1/s	1180 1/s	2300 1/s	1180 1/s
E_{pyr}	60,300 J/mol [30]	65,800 J/mol	65,800 J/mol	62,500 J/mol	65,800 J/mol
char model	Eq. 11	Eq. 11	Eq. 12	Eq. 12	Eq. 12
A_{char}	430 m/s [30]	430 m/s [30]	465 kg/(m^2 s) [32]	465 kg/(m^2 s) [32]	465 kg/(m^2 s) [32]
E_{char}	74,800 J/mol [30]	74,800 J/mol [30]	68,000 J/mol [32]	68,000 J/mol [32]	68,000 J/mol [32]
β_{char}	0.2 [30]	0.2 [30]	-	-	-
Δh_{char}	−12 MJ/kg [30]	−12 MJ/kg [30]	−12 MJ/kg [30]	−12 MJ/kg [30]	−32 MJ/kg [33]
$\nu_{O_2,\text{char}}$	1.65 [30]	1.65 [30]	1.65 [30]	1.65 [30]	2.66 [33]

2.3 Simulation details

All simulations which compared the decomposition models described in the previous section had a fuel bed with a depth of $\delta = 8$ cm and a bulk density of $\rho_b = 20$ kg/m^3. However, we also tested

the effect of fuel bed structure in line with the experiments [22]. The alternative fuel bed structures are described in Table 2, where porosity is calculated as $\alpha = 1 - \rho_b/\rho_s$. All bed variations were simulated using the *DM3* decomposition model, which was chosen after having evaluated the predictions of mass loss rate.

Table 2. Summary of the five fuel bed configurations simulated. Variations were made either to bed depth, δ, and/or bulk density, ρ_b, (and by extension porosity, α). All simulations which varied bed structure were conducted with the *DM3* decomposition model.

Simulation	δ **(cm)**	ρ_b **(kg/m^3)**	α **(-)**
Bed1	8	20	0.969
Bed2	6	20	0.969
Bed3	10	20	0.969
Bed4	8	15	0.977
Bed5	4	40	0.938

Additional properties of the vegetative fuel which are required by the model are shown in Table 3. The fuel moisture content of the pine needles was set to 12 % (on a dry mass basis), which is representative of the experimental conditions [22, 25]. The density of the char and ash were estimated from the dry density and the measured yields of these components by assuming negligible shrinking of the particle. Upon reaching complete conversion to ash, particles were removed from the domain. This was done to mimic the loss of bed structure at the trailing edge of the moving front (Fig. 2). A representative gaseous fuel with a composition of $C_{2.1}H_{6.2}O_{2.2}$ was assumed to result from pyrolysis [26, 34], and the heat of combustion was set to 17 700 kJ/kg [21]. The soot yield was set to 0.02 and a radiative fraction of 0.35 was enforced, following Mell et al. [7].

Table 3. Properties of the fuel bed not varied in the simulations (Table 1 or Table 2).

Property	**Value**	**Ref**	**Property**	**Value**	**Ref**
c_{p,H_2O}	4.182 kJ/(kg K)	[35]	ρ_{H_2O}	1000 kg/m^3	[35]
$c_{p,dry,char,ash}$	$\min(2.0, 1.1 + 0.0045\,T_s)$ kJ/(kg K)	[36]	ρ_{dry}	650 kg/m^3	[22, 37]
Δh_{H_2O}	2260 kJ/kg	[30]	σ_s	4660/m	[22, 37]
Δh_{pyr}	418 kJ/kg	[30, 36]	ν_{char}	0.25	[31]
$\epsilon_{H_2O,dry}$	0.98	[38]	ν_{ash}	0.04	[31]
$\epsilon_{char,ash}$	0.75	[39]			

The porous fuel layer was positioned on a flame spread table, which was modeled as a solid obstruction with a log law wall model for representing the tangential velocity in the unresolved

boundary layer. As with the fuel bed, convection is obtained using the maximum of either a free or forced convective coefficient - in this case using correlations for a flat plate. The table interacts with the surrounding radiation field based on a specified emissivity. Heat transfer into the table was modeled using a local 1-dimensional solution to the heat equation and approximate material properties for vermiculite (ρ =700 kg/m^3, c_p =0.94 kJ/(kg K), k =0.19 kW/(m K), ϵ = 0.65). As with the experiment, 2 mm thick sidewalls were also added to restrict the flow, with a height of 3 cm above the height of the fuel bed. These walls were treated numerically in the same way as the table base. Full mathematical details of the treatment of solid boundaries are given in [27]. Ignition was modeled with a thin (5 cm) 20 kW burner activated for 15 s at the start of the simulation.

Fig. 2. Example of (left) experiment and (right) simulation, with particles colored by temperature and fire represented by local heat release rate and soot concentration. This is intended for qualitative illustration only, in order to present the physical scenario under consideration.

The table was set within a domain of 2.40 m by 2.28 m by 1.52 m to provide sufficient distance between the region of interest and any boundary. Boundary conditions were modeled as 'open' due to the large extent of the room surrounding the experiment. This provides a Dirichlet condition for the solution of the Poisson equation for pressure head which is then used to update the velocity field. Temperature and species mass fractions are the ambient initial values if the flow is incoming (due to entrainment) and use values in the grid cell adjacent to the boundary if the flow is outgoing (allowing free advection out of the domain). The boundaries are also open to radiative losses. Details can be found in [27].

For the majority of simulations the outer parts of the domain were resolved with cubic grid cells with a length scale of Δx = 2 cm, while an inner region of 1.60 m by 0.72 m by 1.52 m (centered over the fuel bed) was resolved with cubic grid cells with length scale of Δx = 1 cm. The domain was divided into 46 meshes in order to distribute the computational load across an equivalent number of CPUs. This is shown in Fig. 3.

A key consideration for this choice was the adequate resolution of the solid-phase radiation attenuation: $\Delta x < 4/\sigma_s\beta$ [3]. However, we also conducted a sensitivity study where the grid cell length scale in the vicinity of the fuel bed was varied between Δx = 3 cm and Δx = 0.5 cm. We also tested the sensitivity of the resolution of the radiation solver. In all other simulations, the radiation solver was discretized over 100 solid angles, and the radiation solver is applied to every 5th angle every 3rd time step. In the high resolution case, the solver was discretized over 300

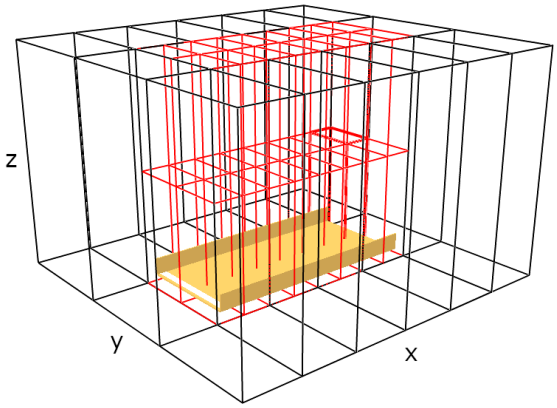

Fig. 3. Subdivision of the numerical domain. The outer meshes (black) had a resolution of $\Delta x = 2$ cm and inner meshes (red) had a resolution of $\Delta x = 1$ cm unless otherwise noted. The outermost boundaries employed an 'open' condition as described in the text.

angles and all angles were updated every time step.

3. Results and discussion

3.1 Effect of thermal decomposition

Mass loss rate was selected as the primary variable of interest for comparing the decomposition models because this is connected not only to the rate of spread (time to consume all fuel) but also to the rate of energy release. The normalized mass loss rates for *bed1* (see Table 2) are shown in Fig. 4 and are compared to the experimental data. The relative degree of fuel consumption is used on the x-axis in order to more clearly show the differences in quasi-steady behavior.

The experiment, which was repeated five times for this fuel bed structure, had an average normalized mass loss rate of $(2.4 \pm 0.5) \times 10^{-3}$/s, taken in the period between 20 % and 80 % of the fuel being consumed. The reported uncertainty is the standard deviation over this period. The average final mass of any un-reacted material was negligible in the experiments. Over the same range of mass consumed, the simulations had average normalized mass loss rates of $(5.8 \pm 0.1) \times 10^{-3}$/s, $(2.8 \pm 0.1) \times 10^{-3}$/s, $(2.7 \pm 0.1) \times 10^{-3}$/s, $(2.9 \pm 0.1) \times 10^{-3}$/s, and $(3.1 \pm 0.1) \times 10^{-3}$/s for *DM1*-*DM5*, respectively. Using the common literature values (*DM1*) resulted in a mass loss rate 2.4 times the experimental mean. Changing the char oxidation model with fixed pyrolysis constants (*DM2* to *DM3*) resulted in a decrease of 4 % in mass loss rate, while fixing the char model and adjusting the pyrolysis coefficients between fits for the two different TGA heating rates (*DM3* to *DM4*) resulted in an increase of 8 %. The uncertainty introduced by the simple method for obtaining kinetic constants is not completely negligible. However, all cases with the pyrolysis model tuned to the TGA data overlap the range of experimental variability, and so this uncertainty may be considered acceptable depending on the application and the uncertainty in other submodels. Changing the char reaction to idealized combustion of carbon (*DM3* to *DM5*) had more of an impact, resulting in an increase of 15 %.

The quasi-steady mass loss rate can also be used as a metric to confirm adequate grid-resolution.

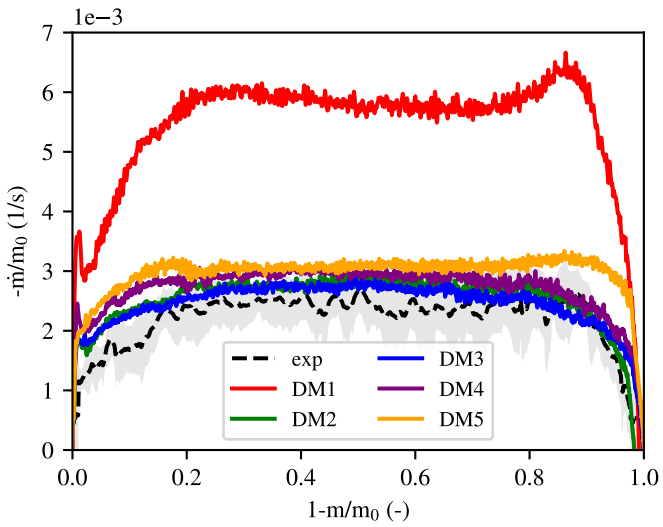

Fig. 4. Normalized mass loss rate versus fuel consumption ratio for the experiment with *bed1* and models *DM1-DM5*. The experiment line is an average of the five repeats, with the shaded region representing the standard deviation.

Fig. 5 shows the effect as resolution is changed from the baseline value (Δx =10 mm). Halving the length scale increased the simulated mass loss rate by 3 % while doubling it increased the prediction by 13 %. Increasing the length scale to 30 mm increased the predicted mass loss rate by 41 % over the baseline value. The additional case with testing the radiation solver (as discussed in Section 2.3) was carried out on an intermediate resolution case (Δx =20 mm) in order to reduce computational cost. Increasing the resolution of the radiation resulted in a change of <0.5 % at the equivalent grid resolution. The finer resolutions predicted mass loss rates within the experimental variability, and the similarity between the baseline and finest resolution demonstrates that the Δx =10 mm grid was an acceptable compromise between accuracy and computational cost.

In addition to the burning rate integrated over the entire surface of the table, the simulations allow examination of the mass loss of individual fuel particles. The evolution of the constituent components from a representative particle is shown in Fig. 6, along with the particle temperature. The particle was located within the bed (0.02 m above the table surface), at the bed centerline, and 0.5 m away from the ignition (where the fire had established quasi-steady spread).

The mass loss rate corresponding to particle ignition is not trivial to determine, but for the sake of comparison we can take the point at which the first 1 % of the dry mass was consumed. For this one representative particle, this corresponds to temperatures of 218 °C, 425 °C, 423 °C, 356 °C, and 464 °C for *DM1-DM5*, respectively. The time to consume the remainder of the dry mass was 4.6 s, 9.5 s, 9.9 s, 7.8 s, and 8.7 s, respectively. The differences in the burning rate of the whole bed can be correlated with lower onset temperatures and more rapid pyrolysis, particularly for *DM1* but also for *DM4*.

The effect of the char reaction rate model is of limited significance at a macro-scale (compare the similarity between *DM2* and *DM3* in Fig. 4) but the assumptions around the heat of reaction and

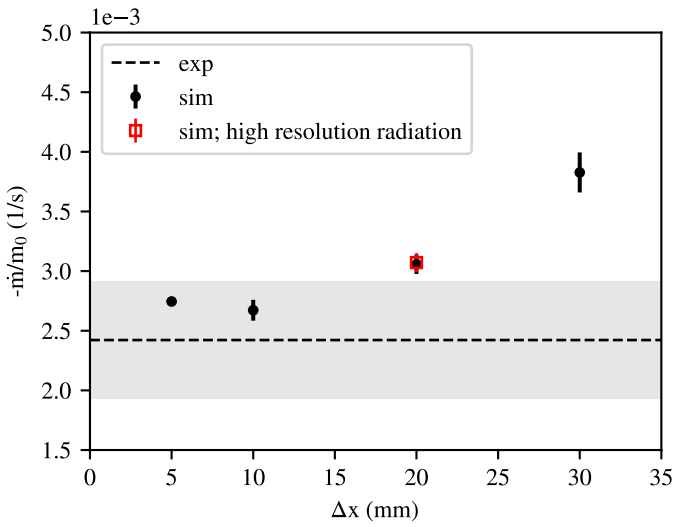

Fig. 5. Quasi-steady normalized mass loss rate as a function of numerical resolution. Values are the average (± standard deviation) over the period of $0.2 \leq (1 - m/m_0) \leq 0.8$.

oxygen stoichiometric coefficient are more important. Greater insight can be gained when comparing at particle scale. The peak temperatures of the exothermic oxidation reaction are 1327 °C, 1186 °C, 916 °C, 911 °C, and 1402 °C, respectively. In addition to higher temperatures when using the previous reaction rate model (Eq. 11), the reactions are more rapid. Interestingly, in *DM1* there is a delay on the order of 10 s between the end of pyrolysis and the onset of char oxidation. With the constants used in *DM1*, the pyrolysis ends at a low temperature compared to the peak of the oxidation reaction and so it takes longer for the feedback from the exothermic reaction to establish. The mass transfer limit of the updated model lowers the peak temperature and prolongs the reaction. However, the case with an increased heat of reaction has the highest temperature. There is also again a delay between pyrolysis and char oxidation. In this case, it is likely related to the increased oxygen requirement which limits overlap of the char oxidation and flaming region and reduces oxygen entrainment from the trailing edge of the char oxidation zone. Peak reaction temperatures for glowing char oxidation in cellulosic materials have been measured in the range of roughly 800 °C to 1100 °C [32, 39, 40]. While the mass transport based model Eq. (12) appears capable of producing more realistic results, particularly in *DM3* and *DM4*, more work is needed to reduce uncertainty around the selection of parameters for the char model, such as the heat of combustion.

3.2 Effect of bed structure

Using the *DM3* decomposition model, the influence of bed structure on flame spread rate was explored. Following Campbell-Lochrie et al. [22, 41], the structure of the bed can be summarized by the dimensionless parameter $\alpha\sigma_s\delta$ (recall that α is the bed porosity, σ_s is the particle surface-to-volume ratio, and δ is the depth of the fuel bed). Campbell-Lochrie et al. [22] showed a linear correlation of spread rate with this parameter over a range of values.

A comparison of simulated to experimental spread rates for several bed structures is shown in

Fig. 7. The simulated spread rates were determined from an average of the local advancement of the flame position determined using a 30 s moving window, over the period of quasi-steady spread. The simulations predict a similar overall relationship, though there is a deviation for the lowest value of $\alpha\sigma_s\delta$ tested. The predicted spread in this case falls outside the proposed linear relationship, including the experimental uncertainty as determined determined by a 95 % prediction interval on the fit. A similar trend was observed for the average mass loss rate, but fewer experimental measurements were available for comparison so we focus on the spread rate.

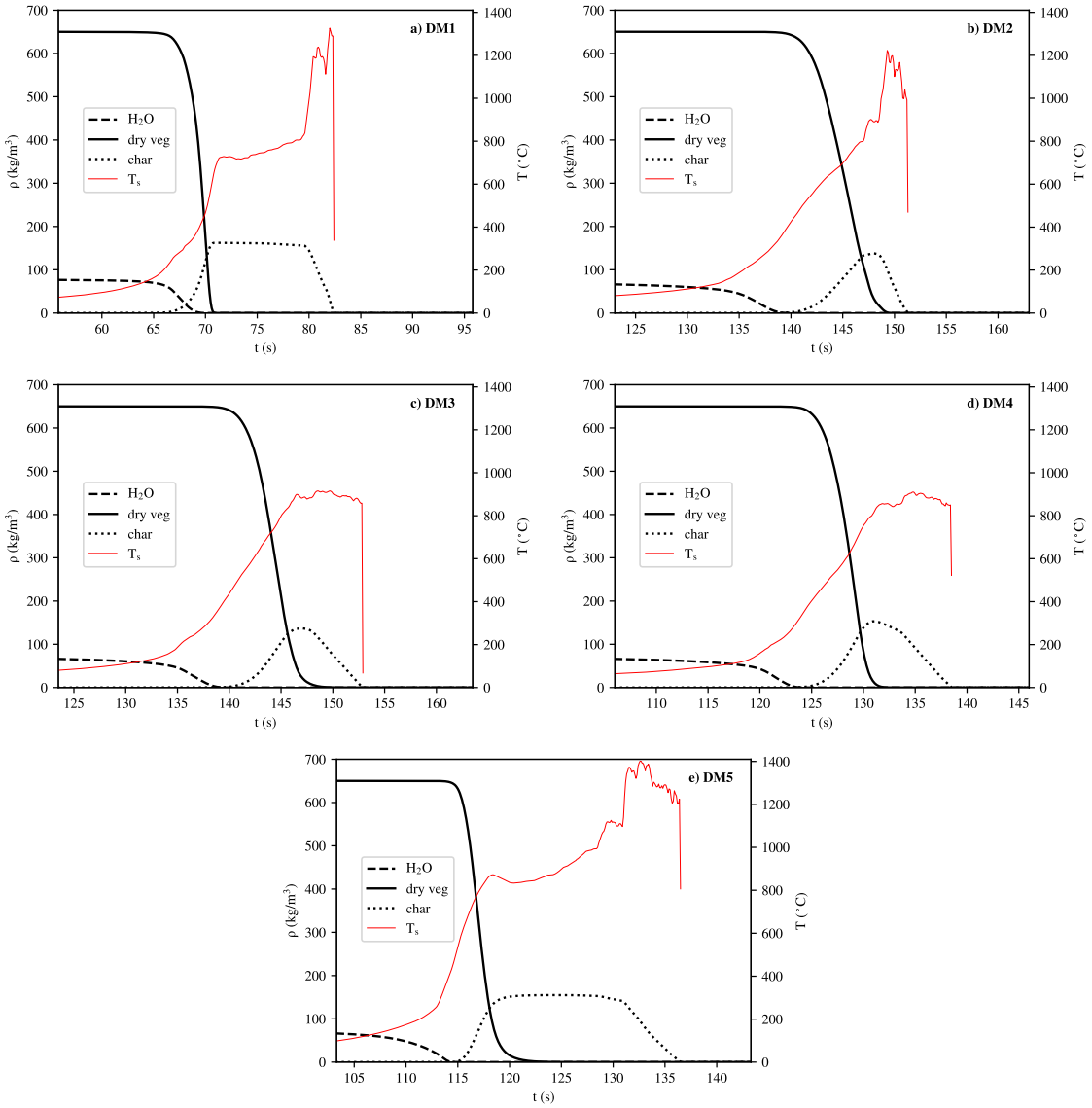

Fig. 6. Response of a single particle within the fuel bed for decomposition models: a-e) *DM1-5*. The black lines represent the density of components of water, dry virgin vegetation, and char, respectively. The ash component is not shown for clarity (comprises only 1 % of the dry mass). The temperature of the particle is shown in red.

It is interesting to note that the simulations qualitatively capture the competing effects of bed

properties. For example, with the 8 cm fuel bed, reducing the bulk density by 25 % reduced the available energy but increased the porosity, resulting in spread which increased by 8 %. On the other hand, also reducing the mass by 25 % by reducing the depth of the fuel bed to 6 cm but maintaining the porosity led to a reduction in spread of 16 %. Maintaining the same mass as the *bed1* case but compacting it to half the depth reduced the predicted spread by roughly 50 %. However, as noted above, this value deviates somewhat from the experimental trend. The depth of the fuel in this case begins to approach the grid resolution (only 4 cells across the depth of the bed) and so numerical sensitivity may play a more significant role. More work is needed to understand the effect of resolution as a function of bed properties. In addition, it was observed that for the lowest fuel loading the behavior was dominated by flame spread between individual needles which is unresolved in this modeling approach. Nevertheless these are encouraging results for demonstrating the ability of the model to capture the importance of bed structure at higher loadings and bulk densities.

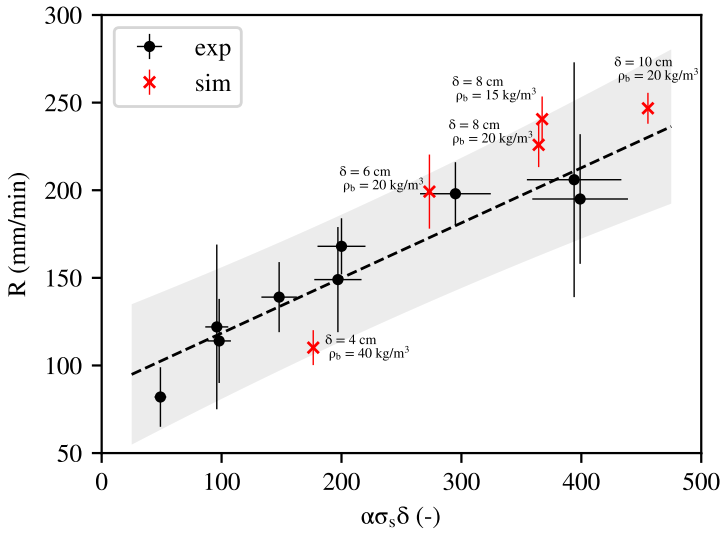

Fig. 7. Flame spread rate as a function of bed structure ($\alpha\sigma_s\delta$). Experimental error bars represent the standard deviation of multiple repeats and the uncertainty in particle properties [22], and the shaded area represents a 95 % prediction interval on a linear fit. Simulation error bars represent the standard deviation during the period of steady spread.

3.3 Heat flux predictions

Radiative heat flux was measured in the experiments at a number of locations. Of particular interest are those made at the surface of the table (bottom of the fuel bed) and the top of the fuel bed, with an upward-looking orientation. The measurements give an indication of the magnitude and duration of heating from the combined fuel bed and flame zone and from the flame zone only, and they are useful for checking the representation in the model. Here we compare to simulations of *bed1* (Table 2) with model *DM3* (Table 1).

The time histories of the heat fluxes are shown in Fig. 8. For the sake of comparison, experiment and simulation times have been adjusted to the respective arrival of the fire. As the sapphire

windows transmit only in the range of roughly 0.2 to 5.5 µm, an additional error estimate is shown to account for the potential to miss longer wavelength radiation. For example, from a graybody emitter at 1200 K (representative of the char oxidation) roughly 25 % of the radiative energy is emitted above 5.5 µm and may be excluded by the window [35]. This error estimate is only a rough approximation as it simplifies both the spectrum of emission and transmission, but it gives some indication of the potential uncertainty in the measurement.

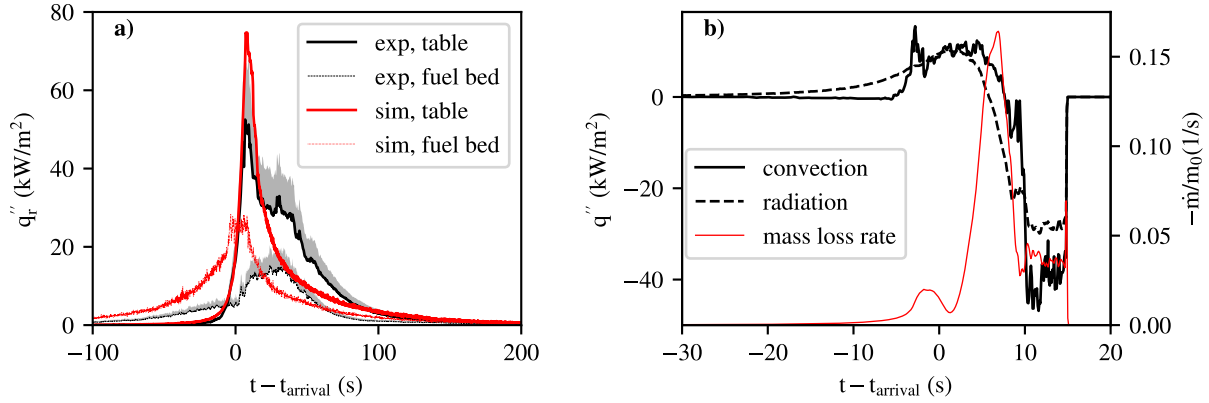

Fig. 8. (a) Radiative heat flux at table surface and upper surface of the fuel bed. (b) Net convective and radiative flux for the particle shown in Fig. 6c compared to the particle mass loss rate. Times are adjusted relative to the approximate arrival of the flame front.

The simulation over-predicts the peak experimental radiative flux by 42 % at the table surface and 86 % at the upper surface of the fuel bed. However, when estimating the effect of window spectral transmissivity, the predicted peak flux at the table surface is within 5% of the measurement. The model captures the significant increase in heat flux at the table surface compared to the top of the bed, though this ratio is 2.6 in the simulation compared to 3.4 in the experiment. Unlike the experiment, the model predicts that the peak radiative flux at the top of the bed occurs slightly before that at the base. The degree of uncertainty in experimental gauge position and angle is unknown, and the upper gauge may also locally affect the flame spread (due to the intrusive placement in the fuel bed). However, this may also indicate a discrepancy in the predicted shape of the flame surface, and future investigation may be useful.

A summary of all peak heat flux measurements at the table surface (bottom of the fuel bed) is given in Fig. 9. This summary demonstrates a clear trend in increasing radiative flux with spread rate even with the inherent experimental variability on a case-by-case basis. Simulation values are within the range of the error bars. The tendency to predict high radiative fluxes can be seen but this agrees with the trend given the higher values of predicted spread. The only exception is the simulation which corresponds to the shallow fuel bed. As discussed, the coarser relative resolution means that the bed radiation attenuation is likely not well-resolved and this can help explain the high peak flux despite the slow spread.

The simulated net heat fluxes to the representative target particle are also shown in Fig. 8. Prior to the arrival of the fire the heating is dominated by radiation which begins to drive the drying of the particle. However, the peak of the drying reaction occurs after the arrival of the fire, at which point

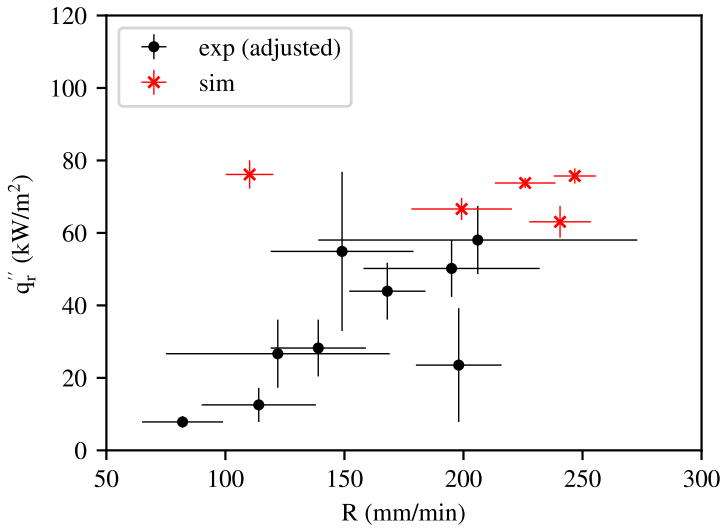

Fig. 9. Peak radiative heat flux at the table surface (bottom of the fuel bed) as a function of bed structure ($\alpha\sigma_s\delta$). Values are from a 1-second moving average and are adjusted for window transmission band, as described in the text. Experimental error bars represent the maximum deviation of multiple repeats and the uncertainty in particle properties [22, 41]. Simulation error bars also represent the maximum deviation from an average of three samples obtained within the fuel bed.

surrounding gas-phase conditions produce convective heating on the same order of magnitude as the radiation. The maximum values are 15 kW/m^2 and 11 kW/m^2 for convection and radiation, respectively. As the particle pyrolyzes and then begins to oxidize it increases in temperature, both net fluxes reach large negative values, with minimums of -47 kW/m^2 and -30 kW/m^2, respectively. It is interesting to note that the balance between the particle cooling and the exothermic char oxidation will affect the temperature and duration of the smoldering. The model proposed for convection (and by extension the mass transfer coefficient for oxygen) considers an ideal configuration of the bed which may not hold as the burning bed begins to collapse, and the sensitivity to this parameter may also be worth considering in future.

4. Conclusions

A CFD model with a multiphase approach was used to simulate flame spread in pine needle beds in quiescent conditions. An evaluation of coefficients used to model drying and pyrolysis thermal decomposition indicated the possibility of significant sensitivity. If fuel-specific information is not available this work demonstrated the potential for a discrepancy of a factor of 2.4 in the predicted mass loss rate, when compared to experimental measurements. Sensitivity to fitting kinetic pyrolysis parameters A and E to limited data (i.e. a single heating rate from TGA test) was also explored, but the effect on mass loss rate was less significant (change of 8 %). A diffusion-based approach for modeling the rate of char oxidation was also tested. The impact on global mass loss rate was small (4 %), but the temperature and duration of the smoldering were more realistic. Additionally increasing the char heat of combustion and mass stoichiometric coefficient of oxygen

to assume combustion of pure carbon had a more significant impart on mass loss rate (15 %). However, these parameters, as well as the kinetic parameters for char oxidation, are still not based on direct measurement of the specific fuel under relevant conditions so more work is needed to evaluate this simple char model.

These results must also be viewed as scenario-specific. For example, the importance of wind in certain fire spread scenarios may dominate over the sensitivity to the decomposition models. Nevertheless, these findings indicate the consideration which must be given when selecting model parameters. The effect of using more detailed pyrolysis models, such as with oxidative pyrolysis, can be explored in future work.

Finally, numerical predictions from one of the thermal decomposition models were evaluated against experimental observations in more detail to interrogate the ability to capture the relevant processes. Despite the overall simplicity of the selected approach, the model was able to qualitatively represent the role of fuel bed structure on flame spread rate. Likewise, investigation of heat fluxes showed qualitative agreement in the relationship between radiation and spread rate and the significant contribution of in-bed compared to above-bed radiation. This exercises demonstrates the potential of the model as a tool to independently explore chemistry and structure effects in a systematic and controlled manner.

5. Acknowledgements

We wish to thank Dr. Randy McDermott and Dr. Kevin McGrattan for their valuable insight throughout this work. We also thank Dr. Nicholas Skowronski and Dr. Michael Gallagher of the US Forest Service and acknowledge the Strategic Environmental Research and Development Program (SERDP) for supporting the experimental work upon which this study relied (grant RC-2641).

References

[1] Anatoliĭ Mikhaĭlovich Grishin. *Mathematical modeling of forest fires and new methods of fighting them*. Publishing house of the Tomsk State University, Tomsk, Russia, 1997.

[2] M Larini, F Giroud, B Porterie, and J-C Loraud. A multiphase formulation for fire propagation in heterogeneous combustible media. *International Journal of Heat and Mass Transfer*, 41(6):881–897, 1998.

[3] Dominique Morvan. Physical phenomena and length scales governing the behaviour of wildfires: A case for physical modelling. *Fire Technology*, 47(2):437–460, 2011.

[4] E Pastor, L Zarate, E Planas, and J Arnaldos. Mathematical models and calculation systems for the study of wildland fire behaviour. *Progress in Energy and Combustion Science*, 29(2):139–153, 2003.

[5] William Mell, Mary Ann Jenkins, Jim Gould, and Phil Cheney. A physics-based approach to modelling grassland fires. *International Journal of Wildland Fire*, 16(1):1–22, 2007.

[6] Andrew L Sullivan. Wildland surface fire spread modelling, 1990–2007. 1: Physical and quasi-physical models. *International Journal of Wildland Fire*, 18(4):349–368, 2009.

[7] William Mell, Alexander Maranghides, Randall McDermott, and Samuel L. Manzello. Numerical simulation and experiments of burning douglas fir trees. *Combustion and Flame*, 156(10):2023–2041, 2009.

[8] Ambarish Dahale, Selina Ferguson, Babak Shotorban, and Shankar Mahalingam. Effects of distribution of bulk density and moisture content on shrub fires. *International Journal of Wildland Fire*, 22(5):625, 2013.

[9] Y. Perez-Ramirez, W. E. Mell, P. A. Santoni, J. B. Tramoni, and F. Bosseur. Examination of WFDS in Modeling Spreading Fires in a Furniture Calorimeter. *Fire Technology*, 53(5):1795–1832, 9 2017.

[10] Mohamad El Houssami, Aymeric Lamorlette, Dominique Morvan, Rory M. Hadden, and Albert Simeoni. Framework for submodel improvement in wildfire modeling. *Combustion and Flame*, 190:12–24, 4 2018.

[11] Dominique Morvan, Gilbert Accary, Sofiane Meradji, Nicolas Frangieh, and Oleg Bessonov. A 3D physical model to study the behavior of vegetation fires at laboratory scale. *Fire Safety Journal*, 101:39–52, 10 2018.

[12] O. P. Korobeinichev, S. Muthu Kumaran, D. Shanmugasundaram, V. Raghavan, S. A. Trubachev, A. A. Paletsky, A. G. Shmakov, R. K. Glaznev, A. A. Chernov, and A. G. Tereshchenko. Experimental and Numerical Study of Flame Spread Over Bed of Pine Needles. *Fire Technology*, 2021.

[13] O. P. Korobeinichev, S. Muthu Kumaran, V. Raghavan, S. A. Trubachev, A. A. Paletsky, A. G. Shmakov, R. K. Glaznev, A. A. Chernov, A. G. Tereshchenko, E. L. Loboda, and D. P. Kasymov. Investigation of the Impact of Pinus Silvestris Pine Needles Bed Parameters on the Spread of Ground Fire in Still Air. *Combustion Science and Technology*, pages 1–23, 2022.

[14] Mohamed M Ahmed, Arnaud Trouvé, Jason M Forthofer, and Mark A Finney. Large eddy simulations of the structure of spreading line fires at flame scale. In Domingos Xavier Viegas and Luis Mario Ribeiro, editors, *Advances in forest fire research*, pages 283–288. Imprensa da Universidade de Coimbra, Coimbra, Portugal, 2022.

[15] Eric V Mueller, Nicholas S Skowronski, Kenneth L Clark, Michael R Gallagher, William E Mell, Albert Simeoni, and Rory M Hadden. Detailed physical modeling of wildland fire dynamics at field scale-An experimentally informed evaluation. *Fire Safety Journal*, 120:103051, 2021.

[16] Chris Lautenberger and Carlos Fernandez-Pello. A model for the oxidative pyrolysis of wood. *Combustion and Flame*, 156(8):1503–1513, 2009.

[17] Virginie Tihay and Philippe Gillard. Comparison of several kinetic approaches to evaluate the pyrolysis of three Mediterranean forest fuels. *International Journal of Wildland Fire*, 20(3):407–417, 2011.

[18] Elham Amini, Mohammad Saeed Safdari, Nathan Johnson, David R. Weise, and Thomas H. Fletcher. Pyrolysis kinetics of wildland vegetation using model-fitting methods. *Journal of Analytical and Applied Pyrolysis*, 157:105167, 2021.

[19] Peyman Rahimi Borujerdi, Babak Shotorban, and Shankar Mahalingam. A computational study of burning of vertically oriented leaves with various fuel moisture contents by upward convective heating. *Fuel*, 276, 2020.

[20] Isaac T. Leventon, Jiuling Yang, and Morgan C. Bruns. Thermal decomposition of vegetative fuels and the impact of measured variations on simulations of wildfire spread. *Fire Safety Journal*, 137, 2023.

[21] Ronald A Susott. Characterization of the thermal properties of forest fuels by combustible gas analysis. *Forest Science*, 28(2):404–420, 1982.

[22] Zakary Campbell-Lochrie, Carlos Walker-Ravena, Michael Gallagher, Nicholas Skowronski, Eric V Mueller, and Rory M Hadden. Investigation of the role of bulk properties and in-bed structure in the flow regime of buoyancy-dominated flame spread in porous fuel beds. *Fire Safety Journal*, 120:103035, 2021.

[23] Eric V. Mueller, Michael R. Gallagher, Nicholas Skowronski, and Rory M. Hadden. Approaches to Modeling Bed Drag in Pine Forest Litter for Wildland Fire Applications. *Transport in Porous Media*, 138(3):637–660, 2021.

[24] Eric V. Mueller, Michael R. Gallagher, Nicholas Skowronski, and Rory M. Hadden. Convective heat transfer in pine forest litter beds. *International Journal of Heat and Mass Transfer*, 195:123057, 2022.

[25] Zakary Campbell-Lochrie, Carlos Walker-Ravena, Michael R Gallagher, Nicholas S Skowronski, Eric V Mueller, and Rory M Hadden. Effect of Fuel Bed Structure on the Controlling Heat Transfer Mechanisms in Quiescent Porous Flame Spread. In Domingos Xavier Viegas and L M Ribeiro, editors, *Advances in forest fire research*, pages 1443–1448. Imprensa da Universidade de Coimbra, Coimbra, Portugal, 2022.

[26] Kevin McGrattan, Randall McDermott, Marcos Vanella, Eric Mueller, Simo Hostikka, and Jason Floyd. Fire dynamics simulator (Version 6.8.0), User's Guide. Technical report, National Institute of Standards and Technology, Gaithersburg, Maryland, 2023.

[27] Kevin McGrattan, Randall McDermott, Marcos Vanella, Eric Mueller, Simo Hostikka, and Jason Floyd. Fire dynamics simulator (Version 6.8.0), Technical Reference Guide. Technical report, National Institute of Standards and Technology, Gaithersburg, Maryland, 2023.

[28] Marcos Vanella, Kevin McGrattan, Randall McDermott, Glenn Forney, William Mell, Emanuele Gissi, and Paolo Fiorucci. A multi-fidelity framework for wildland fire behavior simulations over complex terrain. *Atmosphere*, 12(2):1–25, 2021.

[29] Hermann Schlichting and Klaus Gersten. *Boundary-layer theory*. Springer, 2016.

[30] B. Porterie, J. L. Consalvi, A. Kaiss, and J. C. Loraud. Predicting Wildland Fire Behavior and Emissions Using a Fine-Scale Physical Model. *Numerical Heat Transfer, Part A: Applications*, 47(6):571–591, 2005.

[31] Carlos Walker-Ravena. *Understanding the Heat Transfer, Pyrolysis and Ignition of Wildland Fuels*. PhD thesis, University of Edinburgh, 2019.

[32] N. Boonmee and J. G. Quintiere. Glowing ignition of wood: The onset of surface combustion. *Proceedings of the Combustion Institute*, 30(2):2303–2310, 2005.

[33] Stephen R Turns. *Introduction to combustion*, volume 287. McGraw-Hill Companies, New York, NY, USA, 1996.

[34] Steven J Ritchie, Kenneth D Steckler, Anthony Hamins, Thomas G Cleary, Jiann C Yang, and Takashi Kashiwagi. The effect of sample size on the heat release rate of charring materials. *Fire Safety Science*, 5:177–188, 1997.

[35] Frank P Incropera, David P DeWitt, Theodore L Bergman, and Adrienne S Lavine. *Fundamentals of heat and mass transfer*. John Wiley & Sons, 2007.

[36] Charles R. Boardman, Mark A. Dietenberger, and David R. Weise. Specific heat capacity of wildland foliar fuels to 434 °C. *Fuel*, 292, 5 2021.

[37] J.C. Thomas. *Improving the understand of the fundamental mechanism that influence the ignition and burning dynamics of porous wildland fuels*. PhD thesis, University of Edinburgh, School of Engineering, Edinburgh, UK, 2016.

[38] M El Houssami, J C Thomas, A Lamorlette, D Morvan, M Chaos, R Hadden, and A Simeoni. Experimental and numerical studies characterizing the burning dynamics of wildland fuels. *Combustion and Flame*, 168:113–126, 6 2016.

[39] David Dewey Evans and Howard W Emmons. Combustion of wood charcoal. *Fire Safety Journal*, 1(1):57–66, 1977.

[40] Dennis K. Kim and Peter B. Sunderland. Fire ember pyrometry using a color camera. *Fire Safety Journal*, 106(April):88–93, 2019.

[41] Zakary Campbell-Lochrie, Carlos Walker-Ravena, Michael Gallagher, Nicholas Skowronski, Eric V. Mueller, and Rory M. Hadden. Effect of Fuel Bed Structure on the Controlling Heat Transfer Mechanisms in Quiescent Porous Flame Spread. *International Journal of Wildland Fire*, pages 1443–1448, 2023.

Supplementary Material

5.1 Comparison of pyrolysis models

The impact of fitting to either a low (5 K/min) or high (35 K/min) heating rate was evaluated by using the model fit parameters (Table 1) to simulate a TGA test which was conducted at an intermediate heating rate of 15 K/min. The results are shown in Fig. 10. The TGA tests show a peak pyrolysis reaction temperature of 334 °C while the model obtained with the low heating rate is at 365 °C and that from the high heating rate is at 308 °C. This shift in the peak is analogous to that described in Section 3.1. A similar discrepancy when fitting a single reaction to a single heating rate was described by Amini et al. [18]. More detailed approaches may be required in cases where the sensitivity dominates the overall model predictions.

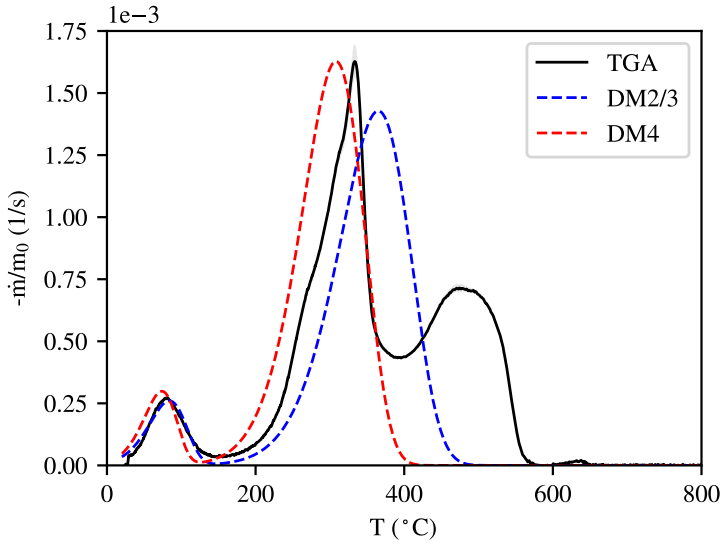

Fig. 10. TGA data at a heating rate of 15 K/min compared to the modeled response with fits from model *DM2/3* (obtained from 5 K/min data) and model *DM4* (obtained from 35 K/min data). Experimental curves are averages of three tests.